Experimental and simulation study of neon collision dynamics with a 1-decanethiol monolayer

N. Isa and K. D. Gibson
The James Franck Institute and Department of Chemistry, The University of Chicago, Chicago, Illinois 60637

T. Yan and W. Hase
Institute for Scientific Computing and Department of Chemistry, Wayne State University, Detroit, Michigan 48202

S. J. Sibener[a)]
The James Franck Institute and Department of Chemistry, The University of Chicago, Chicago, Illinois 60637

(Received 5 May 2003; accepted 29 October 2003)

A study of the energy accommodation of neon colliding with a crystalline self-assembled 1-decanethiol monolayer adsorbed on Au(111) is presented. The intensity and velocity dependencies of the scattered neon as a function of incident angle and energy were experimentally measured. Scattering calculations show good agreement with these results, which allows us to examine the detailed dynamics of the energy and momentum exchange at the surface. Simulation results show that interaction times are, at most, a few picoseconds. Even for these short times, energy exchange with the surface, both normal and in-plane, is very rapid. An important factor in determining the efficiency of energy exchange is the location at which the neon collides with the highly corrugated and structurally dynamic unit cell. Moreover, our combined experimental and theoretical results confirm that these are truly surface collisions in that neon penetration into the organic boundary layer does not occur, even for the highest incident energies explored, 560 meV. © *2004 American Institute of Physics.* [DOI: 10.1063/1.1635805]

I. INTRODUCTION

The energy and momentum exchange of an impinging molecule with a surface is the first step in many surface mediated chemical reactions between adsorbed species. Depending on the degree of energy accommodation, a gas molecule can either scatter or adsorb. No matter what the collisional outcome, momentum exchange must occur where the surface recoils in response to the change of the incident particle's trajectory. Understanding the details of this momentum exchange with the surface's vibrational and rotational degrees of freedom allows one to determine which surface properties lead to efficient gas adsorption. Customizing molecular bond rigidity and the polarization of surface displacements when developing new materials for controlling the extent of momentum transfer in such collisions becomes possible with a thorough understanding of the relevant dynamics of energy and momentum accommodation within the surface. The versatility and ease in manipulating the chemical structure of alkanethiol-based self-assembled monolayers (SAMs) on gold make them nearly ideal systems for systematically probing such questions. As a first approach towards acquiring information behind momentum exchange with intentionally-tailored surfaces, we present information on the collision dynamics of rare gases with crystalline organic monolayers.

Perhaps the biggest advantage for choosing a SAM as the scattering surface is its high crystalline order spanning several hundred Å^2. This makes it possible to compare scattering events from more rigid single-crystal metal surfaces while expanding our understanding of gas–surface interactions with organic and polymer surfaces. Neon was chosen as the collision partner because its inert properties simplify interpretation and calculation while its mass is near the molecular weight of a terminal methyl group. In addition, neon's interaction potential with bound methyl groups can be extracted from known neon-methane interactions that have been experimentally measured and theoretically calculated. During the past five years, theoretical work has been done with the neon/1-hexylthiolate monolayer system to better understand the types of collisions involved in the inelastic scattering and trapping-desorption components using the collision dynamics software package, VENUS.[1–3] As will be shown in this work, the success of VENUS in describing experimental results for neon collisions with self-assembled monolayers makes it a credible simulation code for elucidating scattering dynamics at femtosecond time-scales.

The first rare-gas scattering experiments from SAMs were done with scattered argon impacting amphiphilic monolayers.[4] Dramatic changes in energy transferred to the surface were found to occur when switching from a flurocarbon alkane to a hydrocarbon alkane.[4] Nathanson *et al.* have measured scattering from the disordered surfaces of perfluoropolyether, glycerol, and squalene.[5] The increase in the per-

[a)]Author to whom correspondence should be addressed. Electronic mail: s-sibener@uchicago.edu

centage of the incident energy accepted for each of the three surfaces was ascribed to hard sphere collisions between three different protruding functional groups: CF_x, OH, CH_3. Some preliminary scattering from SAMs supported on evaporated, polycrystalline Au(111) has been reported.[6] Finally, recent argon scattering experiments have been done with alkanethiol monolayers highlighting the effects of simply changing the end group on energy exchange under specific incident conditions.[7] The decrease in fractional energy transferred to the surface when the terminal methyl group was changed to a hydroxyl group was attributed to hydrogen bonding effects laterally restricting alkanethiol chain thermal motions effective in absorbing energy from the incident argon.

The above studies have examined the extent of energy exchange between impinging gas molecules and organic surfaces by measuring the efficiency of this exchange as function of incident energy within a narrow range of incident and final polar angles, together with the use of chemical group modifications. Comparing the amount of energy transferred from slightly modified surfaces can be useful in discerning a likely mechanism behind the scattering dynamics. However, a more definite answer can be ascertained when the system is not only well-characterized (i.e., *in situ* surface crystallinity and cleanliness verified), but also coupled with theoretical calculations showing good qualitative agreement with experimental data collected over a wide range of incident conditions. The agreement of simulation and experiment makes it possible to delineate the key dynamical processes that govern such encounters. Herein we present the first directionally dependent scattering experiments using a single crystal Au(111) substrate combined with extensive numerical simulations to elucidate the energy and momentum exchange dynamics between a rare gas and a crystalline organic overlayer.

A standing-phase 1-decanethiol monolayer on gold was chosen as an ideal system because of the ease in preparing large crystalline domains with well-defined structural properties. The ten-carbon long alkane chains provide the surface with strong intra-chain and much weaker inter-chain forces. This anisotropy is distinct from a metal surface whereby an impinging gas encounters a uniform collection of metallically bonded atoms. We track neon momentum transfer as a function of surface temperature, incident and final polar and azimuthal angles, and incident energy. Extensive VENUS molecular dynamics simulations were also performed to further understand how the orientation of the methylene backbone influences energy and momentum transfer at complex organic interfaces. In this paper, Ne-SAM scattering dynamics will be examined in detail, while in a companion paper, collision-induced SAM excitations will be extensively explored.[8] Together, these two papers develop a comprehensive view of atom-organic interface collision-induced energy and momentum transfer.

II. EXPERIMENT

The inelastic scattering of neon atomic beams from a 1-decanethiol monolayer on Au(111) single crystal was performed using a surface scattering machine described in detail elsewhere; only the salient features will be presented here.[9] Neon atomic beams with various translational energies were made using He and H_2 seeding with nozzles of variable stagnation temperature. The following gas mixtures were used: 110 K neat Ne (19.2 meV, FWHM=3.4 meV), 300 K neat Ne (65 meV, FWHM=16.9 meV), 300 K 5% Ne/He (250 meV, FWHM=24.4 meV), 300 K 1.5% Ne/H_2 (560 meV, FWHM=45.0 meV). A differentially pumped quadrupole mass spectrometer detector with 1° angular resolution rotated around the crystal, its arc defining the scattering plane for detected atoms. The crystal mount was also adjustable for azimuthal direction relative to this plane. Chopper wheels were positioned both before and after the surface to measure initial and scattered neon velocity distributions. The post-crystal chopper was always used in the cross-correlation mode for optimal signal intensity. Scattering data were always collected in the sagittal plane.

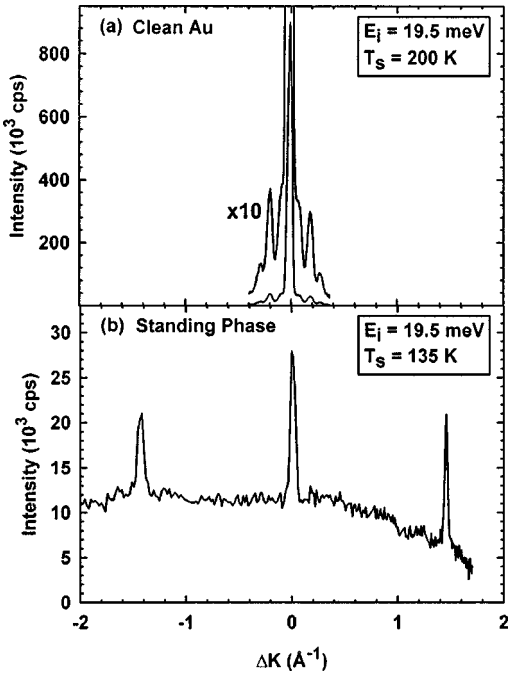

FIG. 1. Helium diffraction scans along the Au⟨110⟩ direction, $\phi_i=0°$, $\theta_i=45°$. (a) Clean Au and (b) 1-decanethiol standing phase.

The Princeton Scientific Au(111) single crystal was mechanically polished and chemically etched with an iodine/potassium iodide solution and checked by x-ray Laue diffraction before it was mounted inside a UHV chamber with a base pressure of 1.9×10^{-10} Torr. The gold crystal was clipped to a tantalum sheet, which could be cooled to 110 K or resistively heated to 1200 K. The final surface preparation involved the removal of calcium and sulfur impurities through several 1.5 kV argon ion sputter and anneal cycles plus a week-long thermal anneal at 1180 K to minimize the number of surface defects. Au(111) order and cleanliness were confirmed by He diffraction. The gold surface had terraces several hundred angstroms in width. Figure 1(a) shows a typical He diffraction spectrum along the Au⟨110⟩ direction, which is defined as $\phi_i=0°$.

The formation of a 1-decanethiol monolayer was achieved using a novel dosing method. A directed beam was

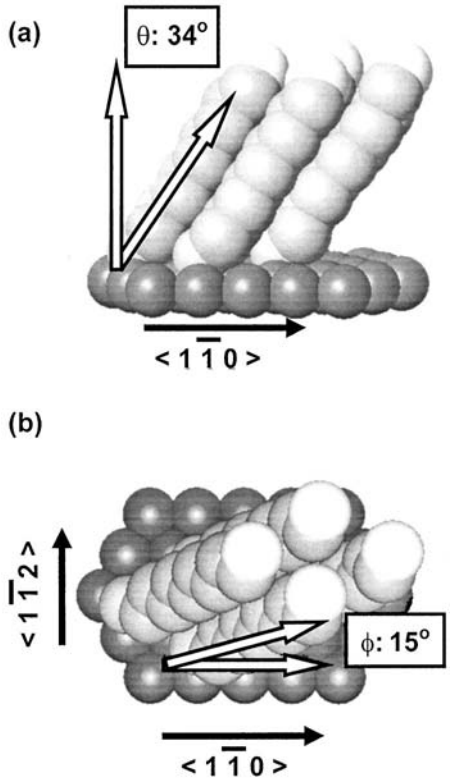

FIG. 2. Side (a) and top (b) views of four 1-decanethiol chains chemisorbed to the Au(111) with the head sulfur group positioned over a gold hollow site. Au(111) lattice vectors, 1-decanethiol tilt ($\theta=34°$) and 1-decanethiol tilt direction ($\phi=15°$) angles are indicated. The united atoms are sized to correspond to the repulsive wall distance extracted from the interaction potential for CH_2-CH_2.

made by bubbling helium through a 1-decanethiol reservoir held at 330 K, followed by supersonic expansion through a 340 K nozzle at a stagnation pressure of 300 Torr. An exposure time of 2 hr was used to dose the 280 K gold crystal forming a $c(4\times2)$ 1-decanethiol monolayer with terraces over several hundred angstroms in width. The He diffraction confirmed the quality of the standing-up phase of the self-assembled monolayer between experimental runs. A typical He diffraction spectrum for the standing-up phase can be seen in Fig. 1(b). The 1-decanethiol monolayer was found to remain unchanged for many days when held at 200 K in the UHV chamber.

III. TRAJECTORY CALCULATIONS

Trajectory calculations were performed using VENUS.[1–3] The 1-decanethiol monolayer surface model consists of 36 1-decanethiol molecules adsorbed on a single layer of 120 Au atoms in the shape of a rhombus. The decanethiol chains have a uniform tilt angle of 34°, an azimuth offset of 15° from the Au⟨110⟩ direction, an all *trans* backbone with $\psi=90°$, and the sulfur head group sits in the hollow site of the Au(111) surface lattice. The standing 1-decanethiol unit cell composed of four chains is shown schematically in Fig. 2, where the united atoms' radii correspond to the repulsive wall distance extracted from the interaction potential for CH_2-CH_2. One improvement in this work from previous VENUS surface calculations is the addition of periodic boundary conditions to efficiently reproduce a larger surface.[10]

Previous experimental and theoretical work has come to the agreement that the $(\sqrt{3}\times\sqrt{3})R30°$ alkanethiol monolayer structure oversimplifies the accepted $c(4\times2)$ lattice with two inequivalent chains per unit cell.[11] However, there is still no general consensus on the specific packing orientation for the $c(4\times2)$ lattice. We decided to start with the simple $(\sqrt{3}\times\sqrt{3})R30°$ monolayer model before adding the additional complexity of the alternating methylene trans-backbone twist angles and different sulfur adsorption sites. Limiting the 1-decanethiol molecules to a single geometric orientation on the Au(111) slab highlights the effects of the incident angle and position in the unit cell at which the neon collides without convoluting the momentum exchange mechanisms with inequivalent sulfur head groups and $-CH_2-CH_3$ tilt angles. Figures 2(a) and 2(b) show side and top views, respectively, of four united-atom 1-decanethiol molecules adsorbed on the Au(111) surface for our simulation model.

As in previous VENUS calculations, a united atom model was used for the methyl and methylene groups of the 1-decanethiol and characterized with the following intramolecular potential:

$$V=\sum_{\text{stretches}}\frac{k_r(r-r_0)^2}{2}+\sum_{\text{bends}}\frac{k_\theta(\theta-\theta_0)^2}{2}+\sum_{\text{dihedrals}}\sum_{n=1}^{3}\frac{k_n[1+\cos(n\phi-\phi_n)]}{2}+\sum_{\text{Lennard-Jones}}\left(\frac{a}{r^{12}}-\frac{b}{r^6}\right). \quad (1)$$

The above parameters used in this study are no different from previous VENUS calculations and can be found in Table I of a previous paper.[3] The intermolecular potential between the incoming neon atom and the tail methyl group of the 1-decanethiol chain is composed of a Lennard-Jones type potential and an exponential repulsion term:

$$V=\frac{a}{r^{12}}+\frac{b}{r^6}+c\exp(-dr)+\frac{f}{r^9}. \quad (2)$$

Equation **(2)** parameter values are based on the nonlinear regression fit to the crossed-beam experimental results[12] between methane and neon, with $a=5.739\text{e}5$ kcal·Å^{12}, $b=-321.12$ kcal·Å^6, $c=1.044\text{e}5$ kcal, $d=3.5638$ Å^{-1}, and $f=-35705$ kcal·Å^9. Comparisons of neon final energy distributions between the above crossed-beam potential and the QCISD(T)/6-311++G** *ab initio* potential showed little difference.[3] SAM–gold interactions are similar to previous VENUS calculations. However, in this paper, the gold atoms are essentially used as a rigid anchoring slab held at their equilibrium positions, i.e., we do not update the gold coordinates during integration of the classical trajectory. This approximation has essentially no impact on the dynamics for this decanethiol system in the energy regime explored in this paper.

Before the trajectory begins, the surface is relaxed to its thermodynamic equilibrium position based on the surface

temperature in the range of 110–200 K. The incoming neon starts ~20 Å above the surface with an incident energy and angle in agreement with an experimental run and is aimed at a unit cell defined by the four central methyl head groups. In Cartesian coordinates, scattering occurs in the xz-plane with the z-axis representing the surface normal vector and $\phi_i = 0°$. Varying the incident azimuthal angle allows us to sample the different 1-decanethiol $\sqrt{3}\times\sqrt{3}R30°$ domains. $\phi_i = 15°$ corresponds to hitting the methyl groups head on with the chain tilt leaning towards the incoming neon. The step size between each iteration is usually 0.5 fs. The neon trajectory is terminated once it again reaches a distance of 20 Å or spends more than 20 ps over the surface. With the exception of 0 K/no zero-point-energy (ZPE) calculations, usually 1000 to 5000 trajectories were collected for each simulation run.

IV. RESULTS AND DISCUSSION

A. Bimodal scattered velocity/energy distribution

After deconvolution of the cross-correlation pattern, the TOF spectra were fit to a sum of two Maxwell–Boltzmann velocity distributions of the form:

$$F(v) = a_1 v^3 \exp\left(\frac{-m(v-v_{01})^2}{2k_B T_1}\right) + a_2 v^3 \exp\left(\frac{-m(v-v_{02})^2}{2k_B T_2}\right), \quad (3)$$

where a_2 or ν_{02} or both might be zero. To delineate whether or not neon trapping followed by thermal desorption occurs, the fitting parameters T_1 and T_2 are allowed to float. For lower energy results, some further asymmetry was added by multiplying a_1 by a series of Hermite polynomials. The quality of the fits, along with the experimental data, can be found in Figs. 3–5. These figures show collections of TOF spectra acquired as a function of incident beam energy (E_i), incident polar angle (θ_i), and final polar angle (θ_f), respectively. In all cases, the reported experimental intensity values are in-plane scattered number density measurements. In Fig. 3, we see that an increase in E_i results in an increase in the average energy of both the fast and slow scattered velocity components. It should also be noted that although the TOF's are fit to a bimodal velocity distribution, the slow velocity peak is not thermalized with the surface. $\langle E_{2f} \rangle$ values are never equal to the surface thermal energy ($2k_B T_s$). As a function of increasing θ_i, there is a noticeable increase in the intensity of the fast scattered component compared to the slow velocity component (Fig. 4). These fast scattered neon atoms tend to leave the surface at glancing final polar angles (Fig. 5).

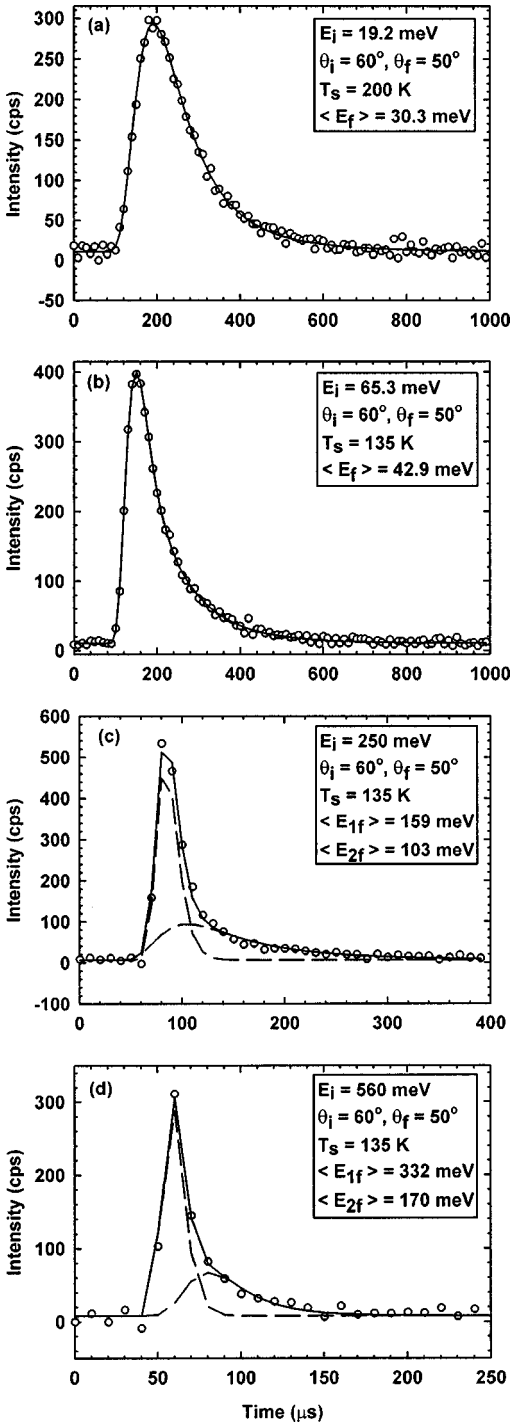

FIG. 3. TOF spectra for different incident Ne energies and fixed incident and final angles ($\theta_i = 60°, \theta_f = 50°, \phi_i = 0°$). Open circles represent the experimental data, solid lines the total fit and dashed lines indicate the fast velocity and slow velocity components; see Eq. (3) in the text. Note that the range of the time axis is varied in these panels to clearly show the bimodal fits.

Figure 6 and Fig. 7 are summary polar plots of the average intensities and $\langle E_f \rangle$, respectively, for many of the TOF data collected at a specified incident energy and surface temperature. From Fig. 6, we see that the angular intensity profile of the scattered neon is dependent on both incident energy and θ_i and can be classified as inelastic lobular scattering in the thermal regime.[13] There is no evidence for neon rainbow scattering even with the lowest surface temperatures and highest incident energies considered. Neon beams with a near normal incidence ($\theta_i = 10°$) have scattered angular distributions which appear to follow a cosine desorption profile for the limited final polar angles accessible with our experimental apparatus (Fig. 6). However, when we track the angular intensity over more glancing θ_f's, the apparent agreement with a $\cos(\theta_f)$ distribution breaks down; i.e., it becomes more lobular. This can be seen clearly when

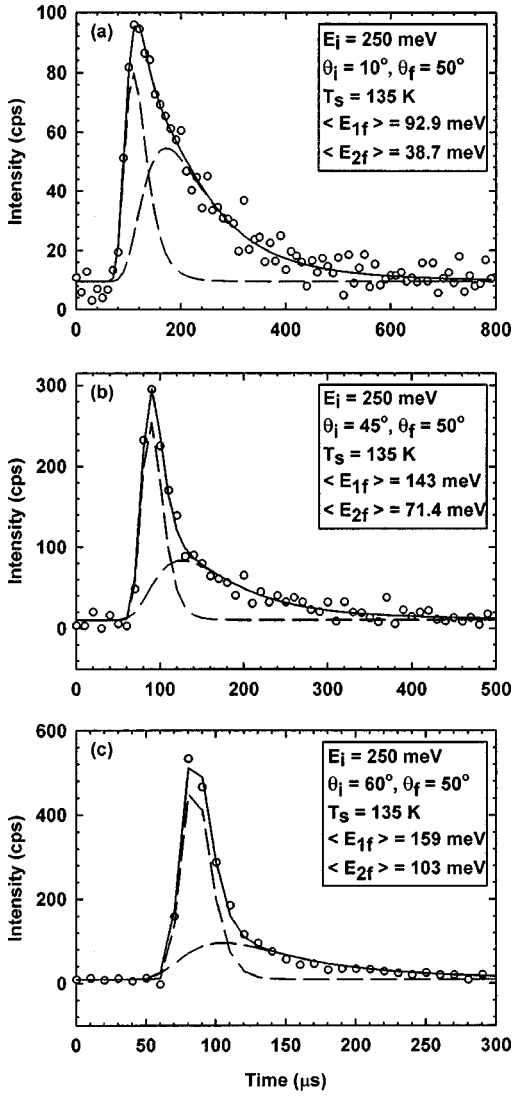

FIG. 4. TOF spectra for different incident Ne polar angles and fixed $E_i = 250$ meV, $\theta_f = 50°$, $\phi_i = 0°$, and $T_s = 135$ K. See Fig. 3 for further details.

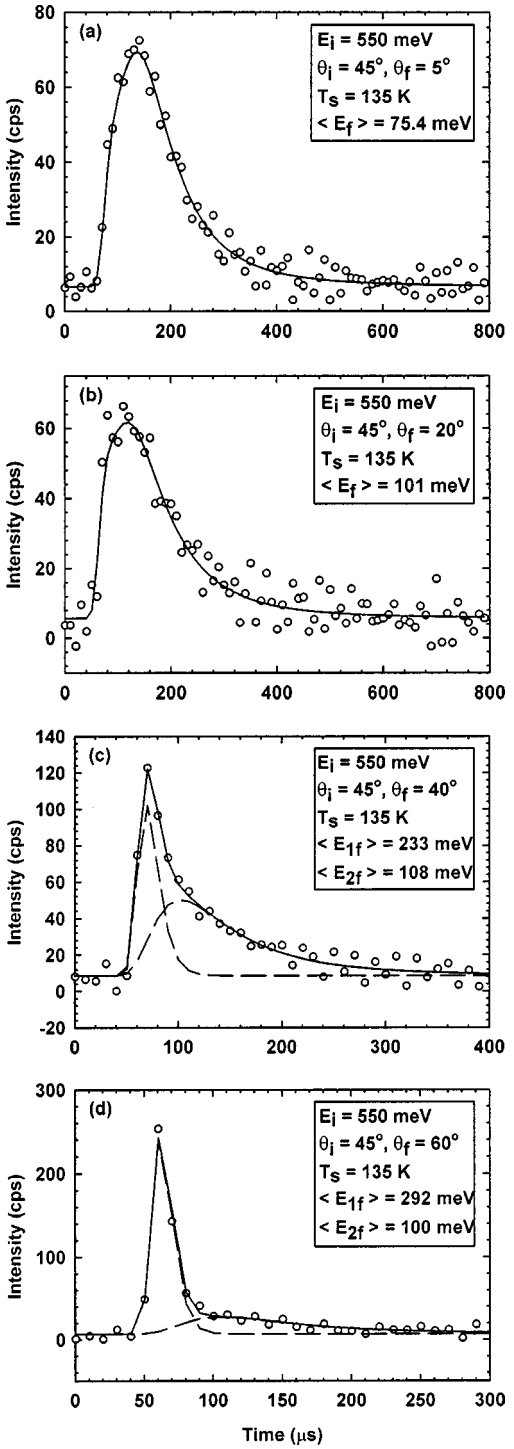

FIG. 5. TOF spectra for different final Ne polar angles and fixed $E_i = 550$ meV, $\theta_i = 45°$, $\phi_i = 0°$, and $T_s = 135$ K. See Fig. 3 for further details.

comparing scattered angular neon intensities with low incident energies and varying incident polar angles [cf. $\theta_i = 10°$, $\theta_i = 60°$ in Figs. 6(a) and 6(b)]. High E_i's and glancing θ_i's results in a greater number of neon scattering superspecularly [cf. $\theta_i = 10°$, 45°, 60° in Fig. 6(c)].

Figure 7 shows the $\langle E_f \rangle$ angular profile dependence on E_i. As seen in Fig. 7(a), an $E_i = 19.2$ meV Ne beam yields identical energy distributions no matter which incident polar angle is chosen. However, once the incident energy is greater than 19.2 meV, the angular energy distribution becomes dependent on both E_i and θ_i [Figs. 7(b) and 7(c)]. The most energetic incoming neon atoms close to the surface normal lose the most energy. The fraction of energy gained or taken from the scattered neon demonstrates how effective the SAM surface is in exchanging energy. For $E_i = 19.2$ meV, the scattered neon gains roughly 10 meV ($\langle E_f \rangle = 31$ meV) from the monolayer without fully thermalizing to the surface temperature of 34 meV ($2k_B T_s$, $T_s = 200$ K). At the same time, neon atoms lose between 20–80% of their energy once E_i is greater than the Ne–surface interaction well but do not leave the surface fully accommodated. In other words, the 1-decanethiol monolayer effectively couples with the incoming rare gas atoms without fully trapping them.

As seen in Fig. 8, the trajectory simulations done with VENUS show good qualitative agreement with the experimentally measured scattered neon energies for a wide range of incident energies and angles. Thermal Maxwell–Boltzmann distributions for each surface temperature are shown with the dashed lines in order to compare scattered neon energy distributions with trapping desorption profiles for fully accommodated events. The data were taken with a well-collimated

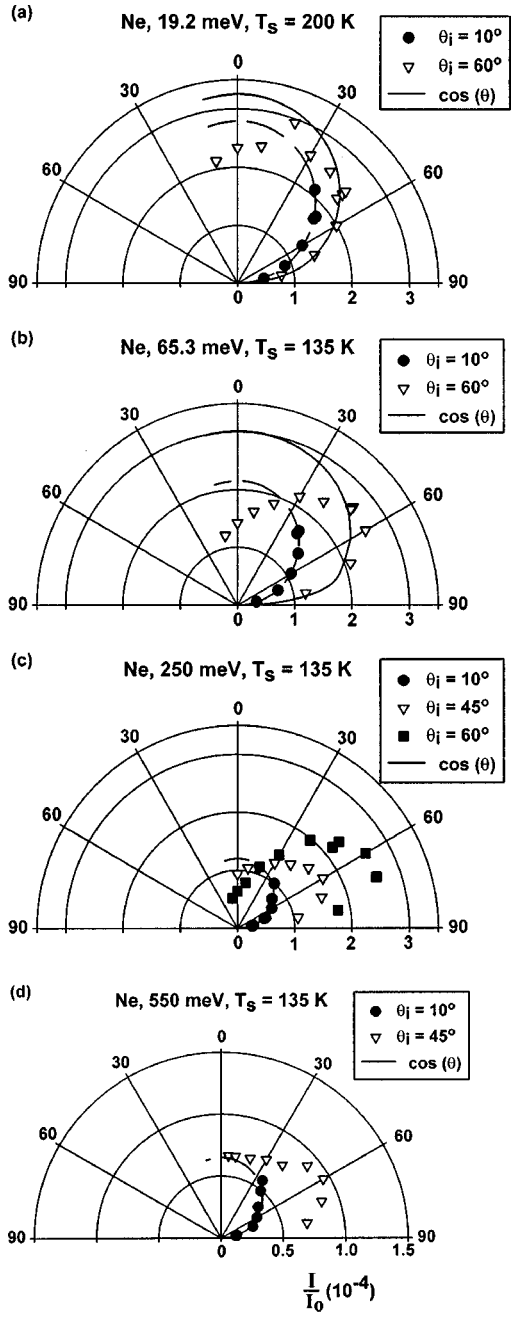

FIG. 6. Normalized intensity (I/I_0) vs final polar angle as a function of incident polar angle and incident energy with fixed $\phi_i = 0°$. Solid lines indicate a cos(θ) distribution.

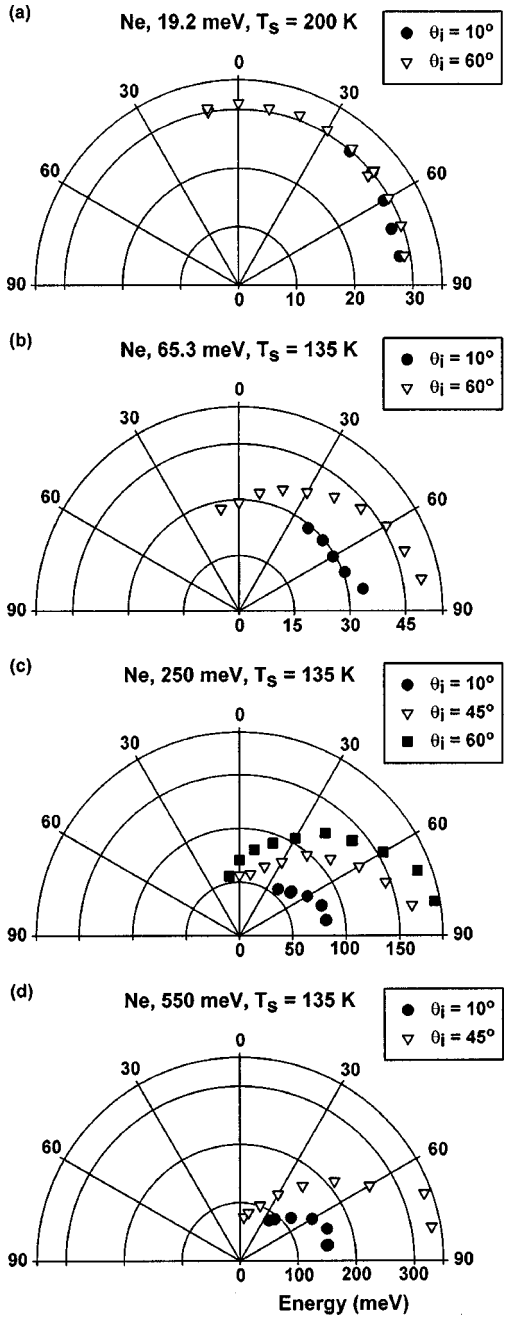

FIG. 7. Final $\langle E_f \rangle$ vs final polar angle as a function of incident polar angle and incident energy with fixed $\phi_i = 0°$.

detector (FWHM$\sim 1°$) at various polar and azimuthal angles. The largest experimental error bars for any experimental data set collected in this work are shown in Fig. 8(d). Reproducing these differential measurements theoretically would have taken many more trajectories than could be reasonably computed. Therefore, a probability comparison is made between the sum of the experimental results and the sum of the trajectory results over the same range of polar angles. A sum of eight experimental spectra with $\theta_f = 0° - 80°$ spaced in 10° increments was used for $\theta_i = 45°$ while for $\theta_i = 60°$, a sum of ten TOF spectra with $\theta_f = -20° - 80°$ was used. In all cases, the experimental initial azimuth was fixed to lie along the Au $\langle 110 \rangle$ direction. Due to the limited number of trajectories computed, the simulation final energy distributions required using a range of out of plane azimuthal angles large enough to give reasonable statistics but small enough so as to not seriously bias the results due to anisotropy of the scattering. Figure 9 shows energy scatter plots from the simulations as a function of θ_f and ϕ_f. With increasing incident energy, many atoms scatter with large final energies, with this being preferentially in the forward scattering direction and in the scattering plane. Overall, the simulations tended to slightly overestimate the fraction of the slow velocity component for $E_i > 100$ meV.

The good qualitative agreement between experiment and simulation means that it is reasonable to use the theory to examine the scattering process in microscopic detail, giving

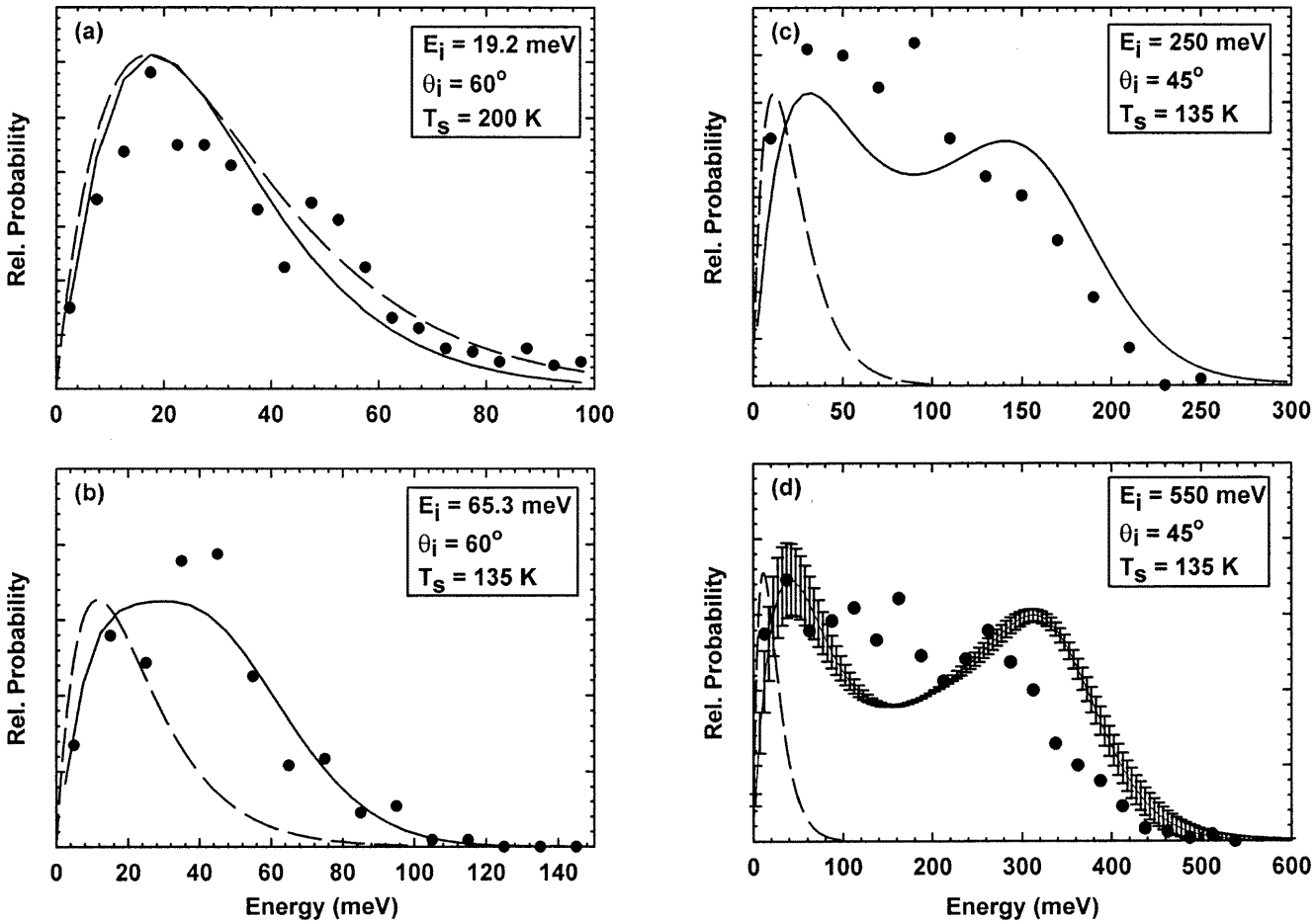

FIG. 8. Comparisons of experimental data with theory over a wide range of incident neon conditions. Solid lines represent a summed average of experimental time-of-flight spectra over all measured final polar angles. Solid circles represent theoretical results. Theoretical results were limited to $\phi_f = 0° - 360°$ for (a) and $\phi_f = 150° - 210°$ in (b)–(d). See the text for further details.

atomic and molecular information at the surface on the femtosecond timescale. Figure 10 gives the Ne–surface interaction time for a wide range of initial conditions. The interaction region extends 5.3 Å above the equilibrium position of the terminal methyl group. An increase in E_i results in a decrease in the median time spent by the neon interacting with the surface: 2.25 ps for 19.2 meV and 0.75 ps for 550 meV. In addition, an increase in E_i results in a decrease in the total number of bounces (see Fig. 11). A single bounce trajectory is defined as having only one z minimum position. Similar to previous literature results, multiple bounces are defined to occur whenever the neon z-velocity vector equals zero and the second derivative is negative.[14] By tracking the neon's energy after each bounce, we can calculate how much energy has been transferred to the surface per neon encounter and determine if and/or when the rare gas has scattered inelastically or undergoes trapping followed by desorption. In general, the neon undergoes very few bounces before scattering; in fact, greater than 60% of the neon trajectories bounce only once or twice before leaving the surface.

Figure 12(a) shows bounce probability profiles in terms of final exit energy and total number of bounces. What is most striking about the neon bounce profile is that one-bounce occurrences have an energy distribution best described by the sum of two Maxwell–Boltzmann distributions and compose the majority of low-energy scattered neon. Figure 12(b) illustrates the energy distribution for single bounced neon atoms with $E_i = 550$ meV, $\theta_i = 45°$, and $\phi_i = 0°$. Fitting the subset of single bounced neon to Eq. (3) results in $v_{01} = 0.118$ cm/μs, $T_1 = 277$ K, $T_2 = 420$ K compared to the experimental fit $v_{01} = 0.135$ cm/μs, $T_1 = 370$ K, $T_2 = 290$ K for $\theta_f = 60°$. The discrepancy between the simulation and experimental v_{01} and T_1 values is due to the simulation's tendency to overestimate the fraction of the slow velocity component. It is not surprising that T_2 is much larger with the simulation fit as compared to the experimental considering that only single bounce trajectories are included.

The slow neon velocity component is composed of trajectories involving both one and several bounces. Figure 13 shows how many bounces are needed until the neon's final energy appears to be thermalized to the surface as a function of E_i. For the lowest E_i considered (19.2 meV), it is found that 2 or more bounces are sufficient to reduce the $\langle E_f \rangle$ to as low as 203 K, a few degrees above $T_s = 200$ K [see Fig. 13(a)]. Moving to a higher E_i (65.3 meV), the number of bounces required for the neon to nearly reach thermal equilibrium increases only slightly to 3 or more bounces. For E_i

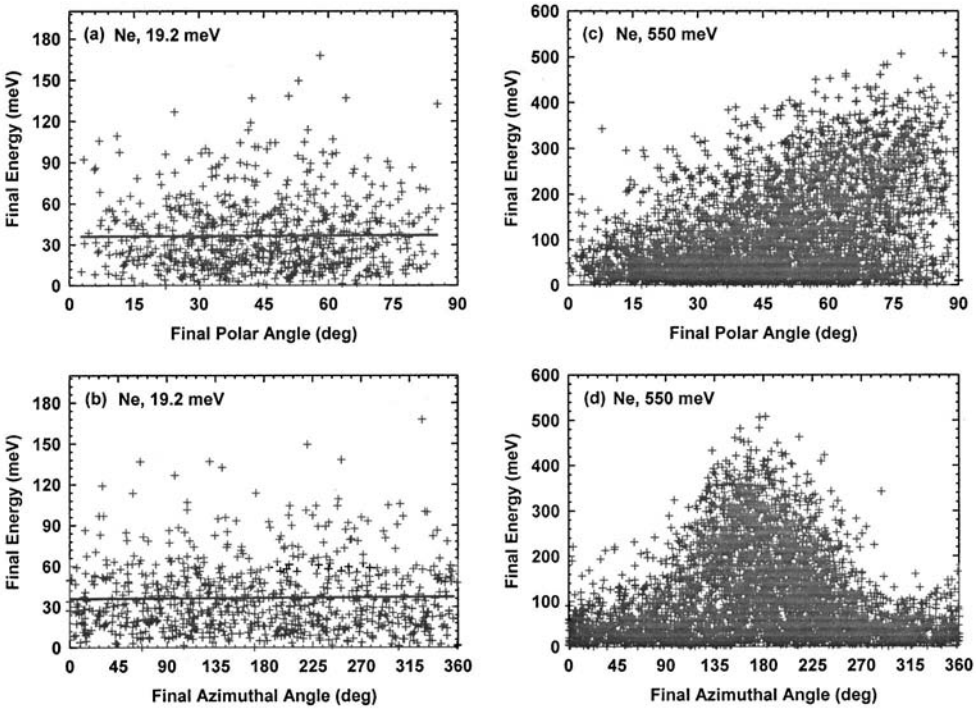

FIG. 9. Final angular energy distributions as a function of incident energy/polar angle. (a) and (b) have initial conditions: 800 trajectories, $E_i = 19.2$ meV, $\theta_i = 60°$, $T_s = 200$ K, $\phi_i = 0°$. (c) and (d) have initial conditions: 4530 trajectories, $E_i = 550$ meV, $\theta_i = 45°$, $T_s = 135$ K, $\phi_i = 0°$. The solid lines are a simple linear fit to emphasize the trends. Each point represents a single trajectory.

above 100 meV, thermalization on average does not occur in the short times the neon is near the surface [see Fig. 13(c)]. In Part C of this section, we will return to this issue of neon thermalization from the viewpoint of parallel and perpendicular momentum accommodation.

Finally, we return to the scattered energy distributions for the lowest neon incident energies studied: $E_i = 19.2$ meV, $\theta_i = 60°$, $\phi_i = 0°$, $T_s = 200$ K. In this case the incident energy is close to the value of the Ne–surface interaction energy ($\sim 10-20$ meV), and less than $2k_B T_s$ (34 meV). Because of the relatively low incident energy, many trajectories are significantly refracted into the well and strike the surface at more normal energies, and at a higher normal velocity than the incoming conditions. This can been seen in Fig. 14 where the trajectory curves towards the surface near its closest approach from the surface for $E_i = 19.2$ meV and not in the 560 meV data. The high surface temperature relative to the well depth implies the neon surface resident time should be low. Indeed, the simulation indicates that most of the atoms interact with the surface for only a few picoseconds. In spite of these factors, the scattered atoms emerge from the surface encounter looking nearly thermalized. This demonstrates the organic overlayer's efficiency in exchanging energy with neon across a wide incident energy regime.

B. Surface temperature effects

Increasing the monolayer surface temperature (T_s) from 110 to 185 K results in a shift in the experimental scattered velocity distribution to faster velocities, i.e., larger $\langle E_f \rangle$ [Fig. 15(c)]. VENUS results followed the experimental $\langle E_f \rangle$ versus T_s trend ($\langle E_f \rangle = 60$ meV/78 meV for $T_s = 110$ K/185 K), as shown in Fig. 16(a). The white arrow indicates how the slow component fraction decreases with increasing T_s while there is a corresponding increase in the fast scattered component as shown by the black arrow. The decrease in neon energy transferred to the surface with an increase in T_s can be explained qualitatively using Baule's hard sphere model. Invoking thermal averaging, whereby the outermost surface atom's initial thermal energy is approximated as $\sim k_B T_s$, the amount of neon energy transferred to the surface ($\delta\varepsilon$) has been shown previously to depend on T_s in the following manner:[15]

$$\delta\varepsilon(T_s) = \frac{4\mu}{(1+\mu)^2}(\varepsilon_i - k_B T_s); \tag{4}$$

μ is defined as the mass ratio of neon atom to the surface atom and ε_i is the incident neon energy. Qualitatively, thermal averaging indicates that energy exchange for surface groups moving away from the neon is not the same as compared with collisions where the methyl groups are moving towards the incident neon at the time of impact. Hence, as temperature increases, the energy exchange decreases. Further support for using such binary collisions to explain our surface temperature effects can be found by analyzing the neon bounce profile as function of T_s. Since the fast scattered component is mainly comprised of single bounce trajectories, one would expect to observe an increase in the number of neon trajectories undergoing a single bounce with an increase in T_s. Indeed, we do see an increase in the relative number of single bounce trajectories with increasing temperature [Fig. 16(b)]. Furthermore, the coupling of the

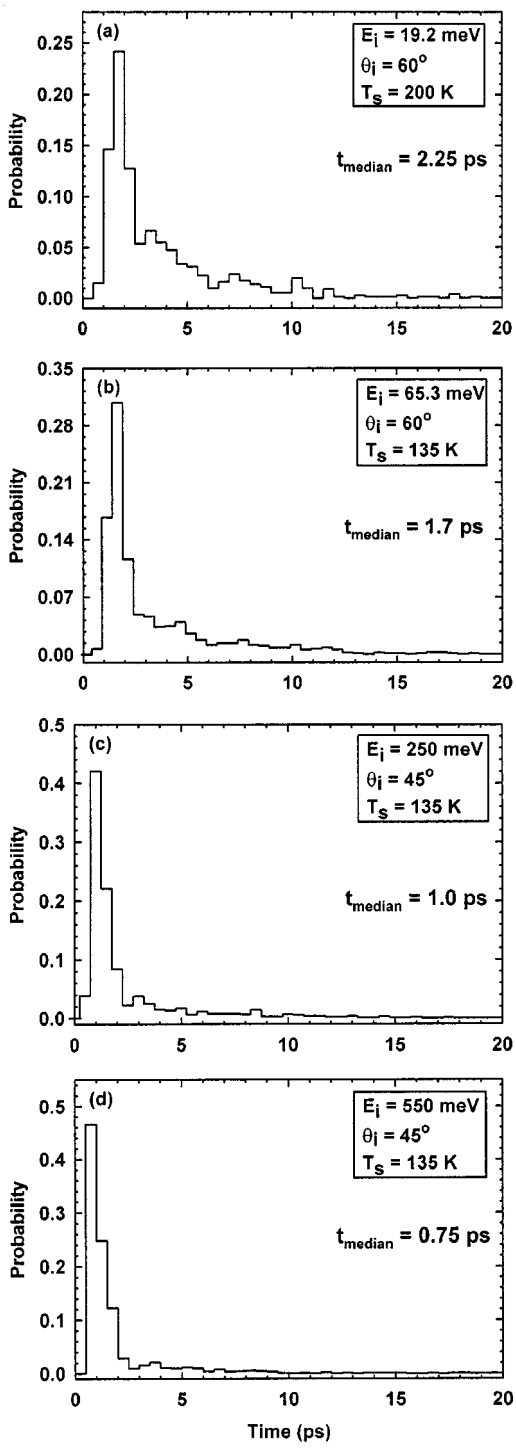

FIG. 10. Ne/surface interaction time as a function of incident Ne energy and incident polar angle: (a) 800 trajectories, $\phi_i = 0°$, $\phi_f = 0° - 360°$; (b) 860 trajectories, $\phi_i = 0°$, $\phi_f = 0° - 360°$; (c) 2060 trajectories, $\phi_i = 0°$, $\phi_f = 0° - 360°$; and (d) 4530 trajectories, $\phi_i = 0°$, $\phi_f = 0° - 360°$.

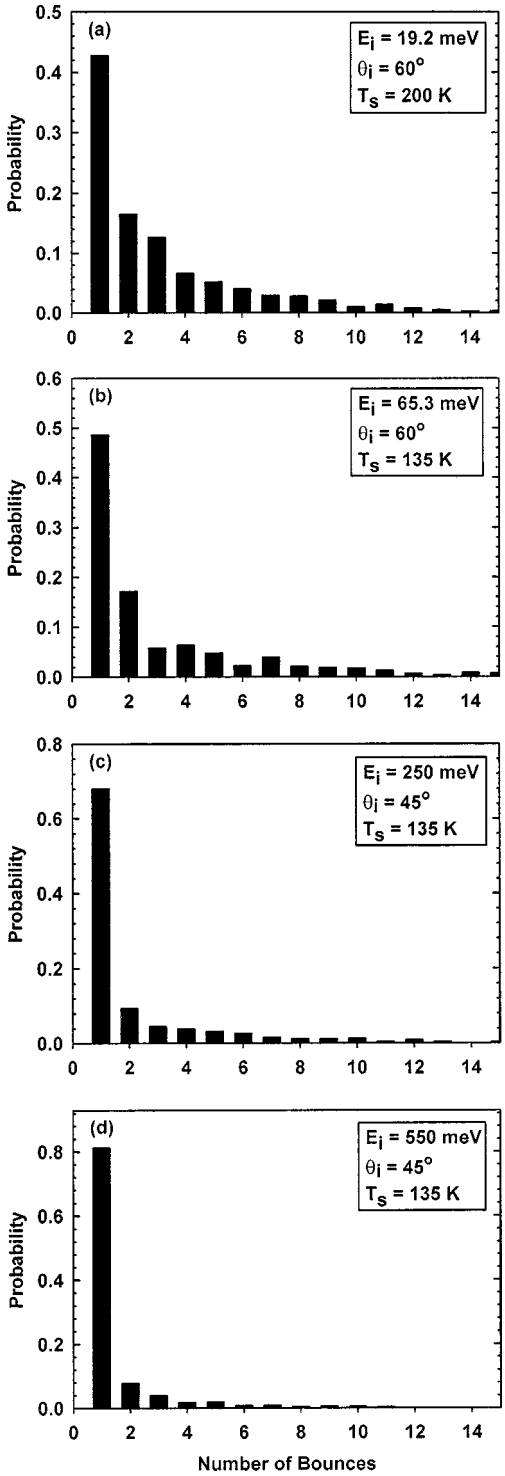

FIG. 11. Bounce number as a function of incident Ne energy and incident polar angle. See Fig. 10 for further details.

Ne-atom translation to the surface motions implies that as the surface temperature is increased, the neon residence time decreases in our statistical model. An increase in T_s results in an increase of the average energy in the Ne-surface dissociation co-ordinate, thus making it more probable for the neon to promptly depart from the surface. This decreased residence time leads in turn, to fewer multiple-bounce trajectories.

C. Parallel and perpendicular momentum analysis

The scattered neon data can be decomposed into parallel and perpendicular momentum components to gain insight into the momentum exchange between the relatively light projectile and a crystalline hydrocarbon surface. A polar plot of perpendicular versus parallel final momentum summarizing the 251 meV neon experimental data as a function of incident angle is shown in Fig. 17(a). $K_{\|}$ is the momentum in

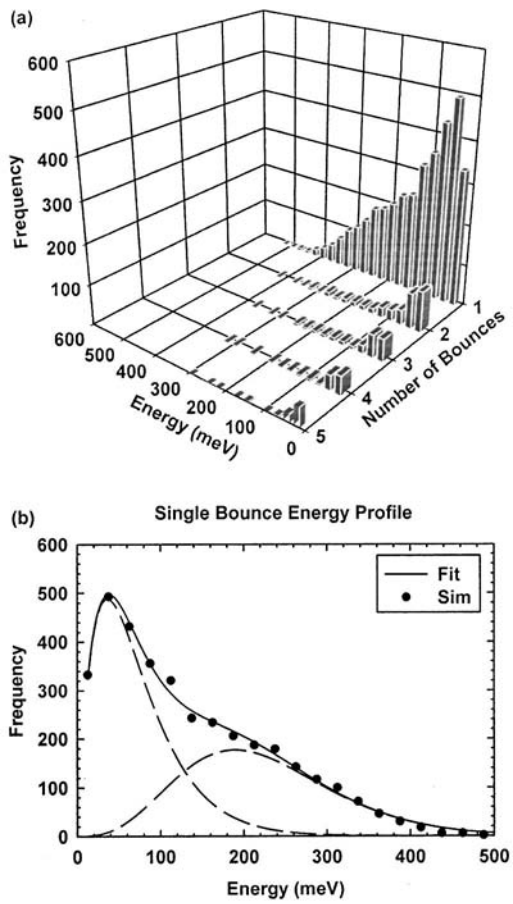

FIG. 12. Energy distributions vs number of bounces from 4530 trajectory calculations. Results shown for 550 meV Ne, $\theta_i = 45°$, $\phi_i = 0°$, $T_s = 135$ K, $\phi_f = 150-210°$. Figure 12(b) shows the energy distribution for only single bounce trajectories. The solid line shows the total fit while dashed lines show the fast and slow component fits; see Eq. (3) in the text.

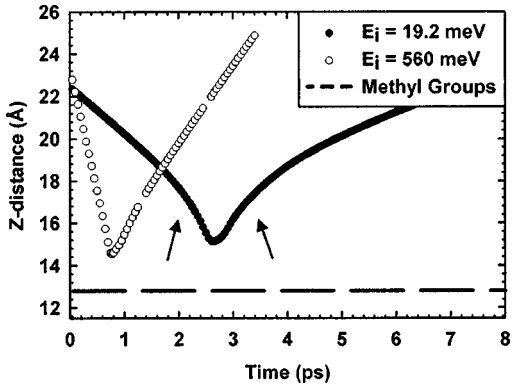

FIG. 14. The z-distance for two neon trajectories vs time is plotted for two different incident energies: (a) closed circles, 19.2 meV Ne, $\theta_i = 60°$, $T_s = 200$ K, $\phi_i = 0°$ and (b) open circles, 560 meV Ne, $\theta_i = 60°$, $T_s = 135$ K, $\phi_i = 0°$. Black arrows indicate at which times and z-distances the low energy neon trajectory is strongly affected by the Ne-methyl group interaction well.

the surface plane and $k_\perp$ is the momentum component perpendicular to the surface. Neon scattered in the sagittal plane with high final energy loses a smaller percentage of parallel momentum than perpendicular momentum; however, in no situation do we see 100 percent conservation of initial perpendicular or parallel momentum [see Fig. 17(b)]. The slow scattered component shows a one-to-one correspondence between $\langle k_\parallel \rangle$ and $\langle k_\perp \rangle$ and little dependence on the initial or final polar angles [Fig 17(c)]. Simulation results with identical initial conditions duplicate the experimental slow component results: $\langle k_\parallel \rangle_{x,f} = 13\ \text{Å}^{-1}$ and $\langle k_\perp \rangle_f = 13\ \text{Å}^{-1}$ ($1\ \text{Å}^{-1} = 6.63E-24$ kg*m/s).

To better understand the exchange of momentum and

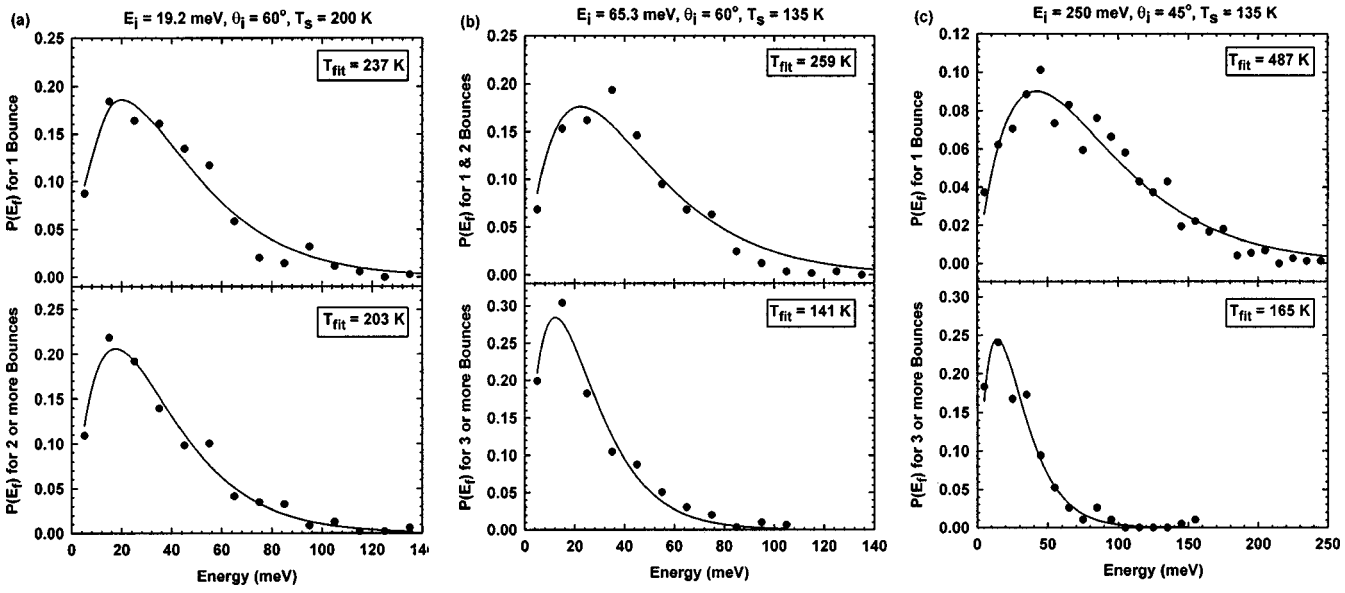

FIG. 13. Ne energy distributions as a function of incident energy and bounce number to show how many bounces are needed for the Ne to nearly reach surface equilibration. Probabilities are determined from the subset of neon trajectories given the specified bounce number in the ordinate label. Temperatures listed in the legends are from Maxwell–Bolztmann fits. See Fig. 10 for further details.

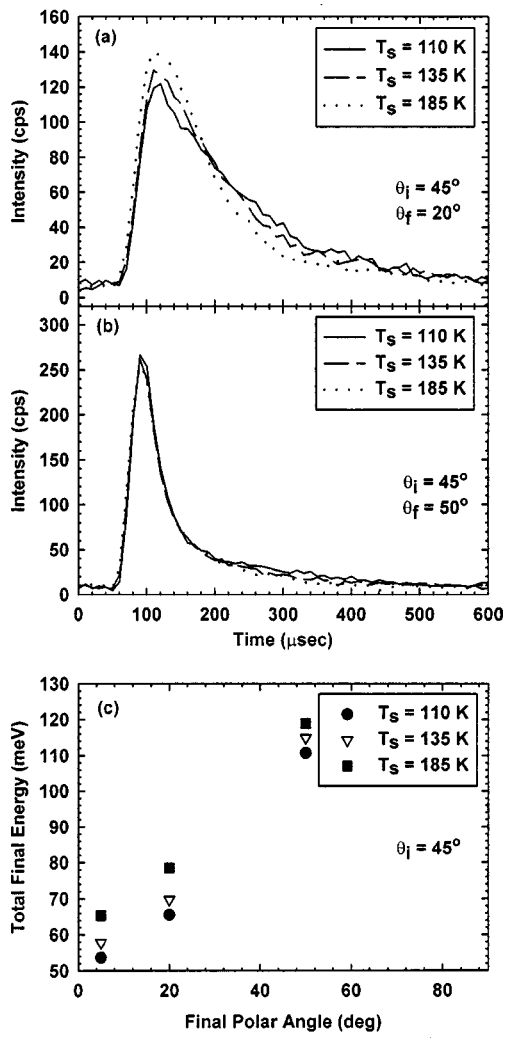

FIG. 15. Experimental temperature dependence for 250 meV neon, $\theta_i = 45°$, $\phi_i = 0°$. TOF spectra for subspecular (a) and superspecular (b) scattered neon as a function of surface temperature. (c) $\langle E_f \rangle$ for scattered neon as a function of the exit polar angle and surface temperature.

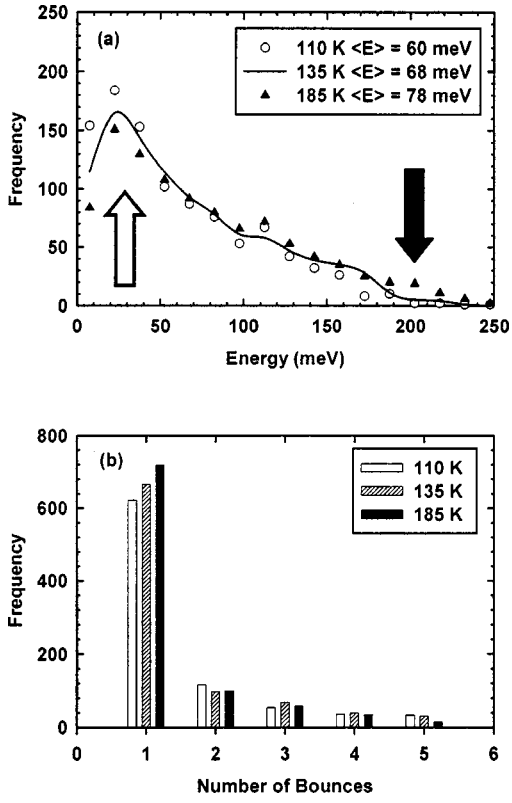

FIG. 16. Simulation results shown for 250 meV Ne, $\theta_i = 45°$, $\phi_i = 0°$, $\phi_f = 0° - 360°$ with 1000 trajectories accumulated for each surface temperature. Exit energy distributions as a function of surface temperature (T_s) are shown in (a). White arrow highlights the decrease in low energy scattering component with increasing T_s. Black arrow indicates an increase in the high energy scattering component with increasing T_s. Bounce number profile as a function of T_s is shown in (b).

energy with the thermal monolayer bath over relatively long periods of time, neon trajectories with initial conditions identical to Figs. 10 and 11 were analyzed in a manner similar to the trapping and desorption work done on Ar–Pt(111).[16] Plotted in Fig. 18 are the neon v_x and v_y distributions as a function of the total bounce number along with the corresponding Boltzmann fit for different incident energies and polar angles. Qualitatively, by determining the tangential neon temperatures and comparing them to T_s, we can predict how quickly the two neon parallel momentum components reach accommodation. Figure 19 shows the scattered neon v_z distributions along with assorted temperatures as calculated from the $\langle E_z \rangle = -k_B T_s$. From these temperature values the degree of perpendicular momentum accommodation can be determined. What we see in all cases, except for $E_i = 550$ meV, is that a very small number of interactions is sufficient for nearly complete energy exchange. Randomizing the energy between the surface and the incoming neon is rapid and efficient. The trends presented here are different from the Ar–Pt(111) work where $\langle k_\perp \rangle$ equilibrated with the surface and $\langle k_\parallel \rangle_x$ and $\langle k_\parallel \rangle_y$ did not. For the Ar–Pt(111) system simulated by Tully and co-workers, having the conditions $E_i = 21$ meV, $\theta_i = 60°$, $T_s = 273$ K, they see very slow thermalization (80–100 ps) of the parallel momentum with rapid equilibration of the normal component of momentum. However, for the Ne/1-decanethiol monolayer system, $\langle k_\parallel \rangle_x$ and $\langle k_\parallel \rangle_y$ reach values near zero for $E_i \leqslant 250$ meV with a median time of ~ 4 ps, the time for 2–3 bounces to occur, as seen in Figs. 18(a) and 18(b). An order of magnitude higher kinetic energy equilibrated in an order of magnitude less time as compared to the Ar–Pt(111) system. The reason for this difference in parallel momentum accommodation is the dramatically different surface topologies between the Pt(111) and 1-decanethiol monolayer.[17] The low energy vibrational mode frequencies for 1-decanethiol monolayer and metal surfaces are nearly identical in energy. The collective alkanethiol wagging motions have calculated low frequency modes from 20–70 cm^{-1} (2.5–8.7 meV).[2] These are similar in energy to measured metal transverse Rayleigh and longitudinal phonon modes in the range of 2–15 meV.[18] Therefore, the facile parallel momentum accommodation for the SAMs case is due to a combination of appropriate frequency modes and the corrugated potential. As will be shown with the subset of single-bounce trajectories scattering from a 0 K surface in Part E of this section, where the neon hits within the unit cell of this highly corrugated surface determines how much energy is transferred to the SAM. Larger total bounce

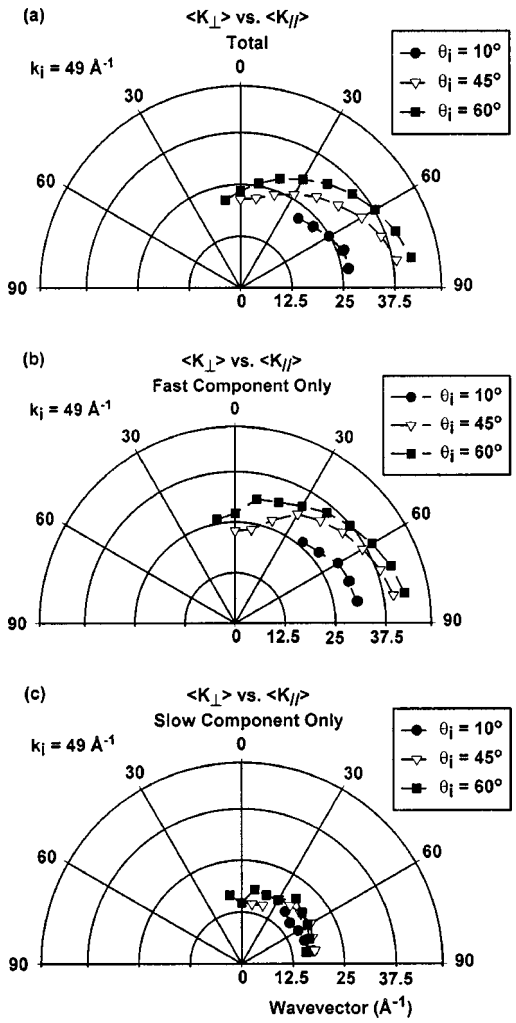

FIG. 17. Parallel vs perpendicular momentum plots for total Ne (a), fast Ne (b), and slow Ne (c), $E_i=250$ meV, $\phi_i=0°$, $T_s=135$ K. Average velocities were calculated from two shifted Maxwell–Boltzmann experimental fits. Radial units are $Å^{-1}$. Lines are a guide for the eye.

numbers implies that the neon has more opportunities to exchange energy with the monolayer. The short interaction time [Figs. 10(c) and 10(d)] and a small number of bounces [Figs. 11(c) and 11(d)] for the translationally more energetic neon ($E_i>100$ meV) scattering from the organic layer is consistent with the nonthermalized final $\langle K_{\|}\rangle_x$ (i.e., in-plane parallel momentum) shown in Figs. 18(c) and 18(d). In these situations, the neon interacts with the chains for a relatively short period of time, and hence does not exchange enough energy to thermalize.

If we consider the subset of neon atoms that scatter after a single bounce, we can qualitatively compare these simulated momentum results to our fast component experimental data shown in Fig. 17(a). From Figs. 18 and 19, we can compare the v_x and the v_z distributions and each of their corresponding temperatures to determine if $k_{\|}$ shows less accommodation compared to $k_{\perp}$, as was seen in the experiment. Since for $E_i \geqslant 65.3$ meV [Figs. 18(b), 18(c), 18(d)], the v_x distributions are nonsymmetric and shifted past zero, we take the v_y temperature as the lower limit for $k_{\|}$ accommodation. Comparing these values to the v_z temperature values we see that the tangential temperature is always higher than the normal temperature: 243 K versus 207 K for $E_i=65.3$ meV, 459 K versus 390 K for $E_i=250$ meV, and 706 K versus 576 K for $E_i=550$ meV. This matches our experimental results. The normal component is more nearly accommodated than the tangential component.

D. Dependence of energy loss on azimuthal orientation

The minor axis of the experimental beam spot is about 1 mm. This encompasses many domains; hence, the experiment samples all of the possible chain orientations simultaneously. We have examined the effect of incident azimuth dependence using VENUS. The 500 neon trajectories each were run in 15° increments from $\phi_i=0°$ to $\phi_i=360°$ with a simulated monolayer composed of a single domain and frozen with no zero point energy at 0 K. Selecting only the fast-scattered neon, the neon exit energy distributions were fit to a Maxwell–Boltzmann energy distribution. $\langle E_f\rangle$ was then calculated from these fits. Although there are some fluctuations in $\langle E_f\rangle$, the overall $\langle E_f\rangle$ does not change significantly as a function of ϕ_i. For this reason, simulation results limited to one initial azimuthal angle compare well with our experimental results. Experimentally, we do observe small azimuth effects with the final energy distributions associated with fast neon measured at glancing final polar angles.

E. Neon energy loss

In order to understand the neon energy distributions, it is necessary to consider how the incoming neon atom exchanges energy with the monolayer. The large number of degrees of freedom in a 1-decanethiol monolayer means that a surface temperature above 100 K yields a very dynamic surface, with methyl groups being tracked traveling a root-mean square (rms) distance of about 0.3 Å during a neon trajectory. For comparison to a coinage metal surface, a rms displacement of 0.09 Å can be calculated from an experimentally measured Ag(111) Debye temperature.[19] The large methylene and methyl groups rms displacements make it difficult to distinguish collision-induced motions from thermal motions of the chains. Therefore, we ran several simulations with an initially static surface and tracked the neon collisions with the terminal methyl groups.

Figure 20 shows the results for two trajectories from the initially static surface simulation. Figure 20(a) pictorially shows the deflection points for these two representative trajectories. The first neon trajectory ($E_i=560$ meV, $\theta_i=45°$, $\phi_i=15°$) scatters in-plane ($\theta_f=53°$, $\phi_f=206°$) with a *low* final energy ($E_f=32.8$ meV). The second neon trajectory has the same initial conditions but scatters in-plane ($\theta_f=71°$, $\phi_f=166°$) with a *high* final energy ($E_f=191$ meV). In the low E_f case, the neon approaches over the hollow site and undergoes a collision with the *side* of a methyl group, losing little energy; however, it is deflected across the hollow site for a second and stronger collision with a neighboring methyl group. For the high E_f case, the collision is with the *top* of the methyl group and the neon scatters into the vacuum. Thus, the neon's final energy is

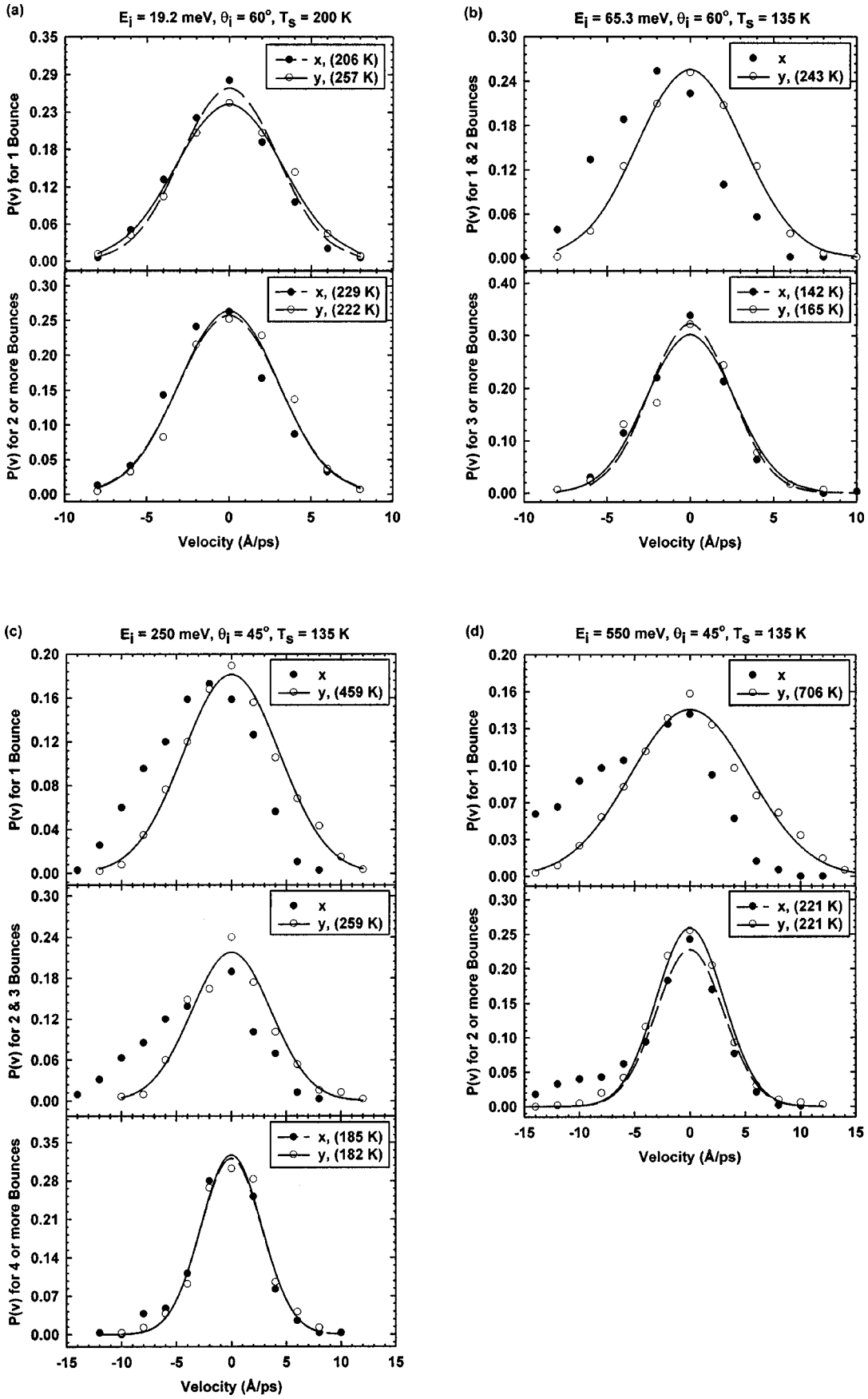

FIG. 18. Final v_x and v_y velocity distributions for different bounce numbers and incident energies. Temperature values are from the fits to Maxwell–Boltzmann velocity distributions (solid lines). See Fig. 10 for more details.

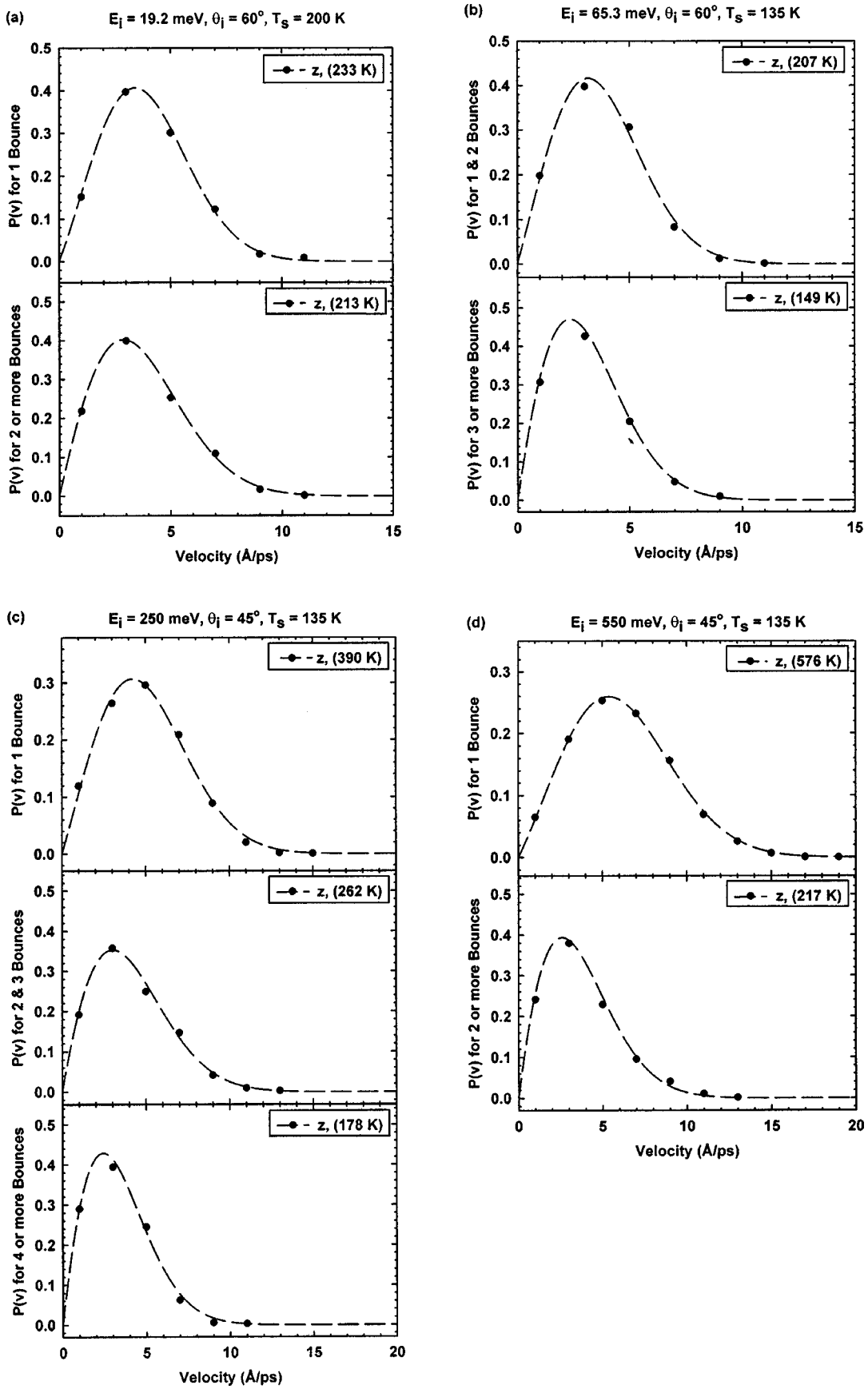

FIG. 19. Final v_z velocity distributions for different bounce numbers and incident energies. The curve fits are done with an arbitrary function. Temperature values are calculated from $\langle E_z \rangle = -k_B T_s$. See Fig. 10 caption for more details.

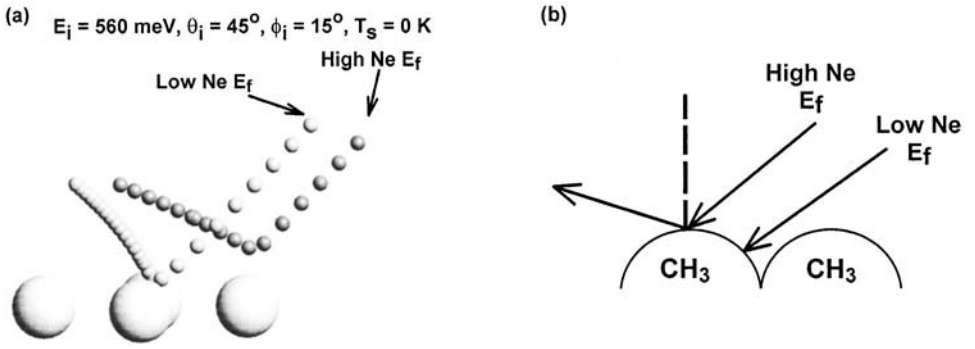

FIG. 20. Results shown for 560 meV Ne, $\theta_i=45°$, $T_s=0$ K, $\phi_i=15°$, $\phi_f=0°-360°$. Panel (a) is a picture of the two trajectories and their four targeted terminal methyl groups. Panel (b) schematically shows the different locations along the methyl surface corrugation that lead to low or high energy exchange. See the text for further details.

highly dependent on the location of impact relative to the methyl head groups. This effect is schematically shown in Fig. 20(b) where both the low and high energy scattered neon approach the surface with the same incident conditions but their final energies are different because of their point of impact.

Previous rare gas scattering studies involving hard metal and semiconductor surfaces have also demonstrated that location of the gas impact within the unit cell determines the final scattered energy.[20,21] Rettner *et al.* found, for example, similar trends for Xe scattering from Pt(111); however, Xe incident energies equal to or above 2 eV were required to sample the metal surface corrugation.[21] This incident energy is well above the highest neon incident energy utilized in this work, 560 meV, and reinforces the fact that the standing-phase 1-decanethiol monolayer is relatively highly corrugated.

The orientation of the chain's backbone with respect to the incoming neon atom makes a small difference on how well the neon transfers/acquires energy from the monolayer. Figure 21 shows the average final kinetic dependence of only one-bounce trajectories as a function of initial azimuthal angle. The difference in energy between a neon atom colliding with a chain tilted towards it ($\phi_i=15°$) versus away from it ($\phi_i=195°$) is roughly 60 meV or $\sim$15% of the total kinetic energy lost. Although the model is not an exact representation of the 1-decanethiol monolayer, these results demonstrate that there is some effect due to chain-tilt orientation.

The experimental results for the scattered neon exhibit qualitatively the hallmark of a simple binary collision; the energy exchange decreases with an increase in the deflection angle ($\theta_i+\theta_f$) (see Fig. 22). For instance, there are three different incident angles shown with an incident energy of 250 meV, but the curves nearly overlap.

Simulations run at realistic surface temperatures show the same effect. This can be seen when tracking the relative positions of the terminal methyl group and the impinging neon. Figure 23 shows, for a fixed incident energy of 550 meV, the final Ne energy as a function of the x and z distances from the closest CH_3 group at the z-turning point. The data in Fig. 23 are for one bounce, where x,z defines the scattering plane, and the solid lines are a linear fit to emphasize the trends. Qualitatively, these demonstrate the different mechanisms for producing fast and slow terminal trajectories. It was found that the neon does not penetrate into the monolayer for the neon incident energy range 19.2–560 meV [i.e., $\Delta z\geqslant 0$ in Fig. 23(a)]. Figure 23(b) shows the final energy as a function of the neon's lateral distance (Δx) from the center of the terminal methyl group at impact. Atoms that scatter with little energy exchange have the smallest, or negative, values of Δx. These are primarily collisions near the top of the methyl groups, which lead to small energy exchange, and, in general, glancing final polar angles. Atoms that hit with larger values of Δx undergo side-on collisions with the methyl groups and then continue to exchange energy with the overlayer as they travel closer to the surface before escaping with a final polar angle near surface normal. To summarize, neon collisions with $\Delta x>0$ lead to higher energy transfer while those with $\Delta x<0$ lead to less energy transfer.

V. CONCLUSIONS

Using a combination of experimental and computational techniques, we have measured and explained the intricate dynamics for neon scattering inelastically from a standing-up phase 1-decanethiol monolayer on Au(111). This work represents a significant step towards developing a quantitative understanding of the mechanisms which govern gas-surface collisional energy and momentum exhange for complex interfaces.

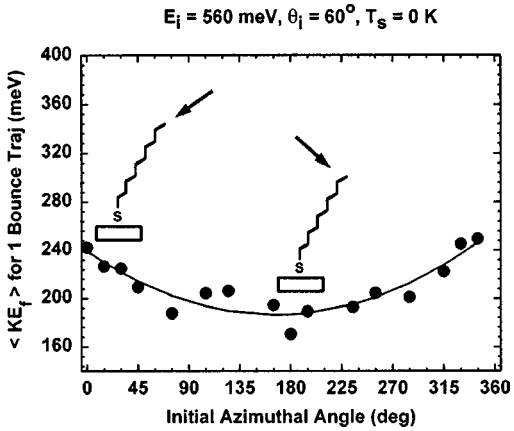

FIG. 21. Final average kinetic energy dependence on azimuthal orientation for single-bounce 560 meV Ne, $\theta_i=60°$, $T_s=0$ K, $\phi_f=0°-360°$. The solid line is a guide for the eye. $\phi_i=15°$ refers to the chain tilting towards the colliding neon and $\phi_i=195°$ refers to the chain tilting away from the incoming neon, as shown by the inserted schematics.

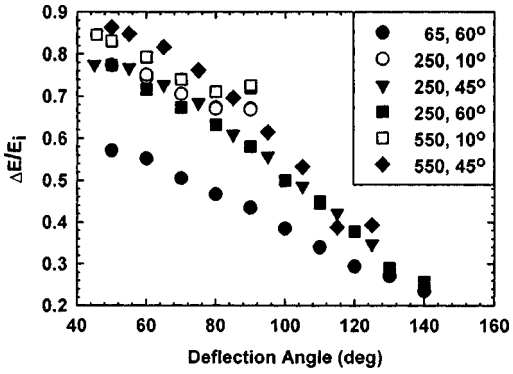

FIG. 22. A plot of $(E_i - \langle E_f \rangle)/E_i$ vs deflection angle $(\theta_f + \theta_i)$ at a fixed $T_s = 135$ K, $\phi_i = 0°$ for six different E_i and θ_i combinations: (a) filled circles, 65.3 meV Ne, $\theta_i = 60°$; (b) open circles, 250 meV Ne, $\theta_i = 10°$; $\phi_i = 0°$; (c) filled triangles, 250 meV Ne, $\theta_i = 45°$, $\phi_i = 0°$; (d) filled squares, 250 meV Ne, $\theta_i = 60°$; (e) open squares, 550 meV Ne, $\theta_i = 10°$; and (f) filled diamonds, 550 meV Ne, $\theta_i = 45°$.

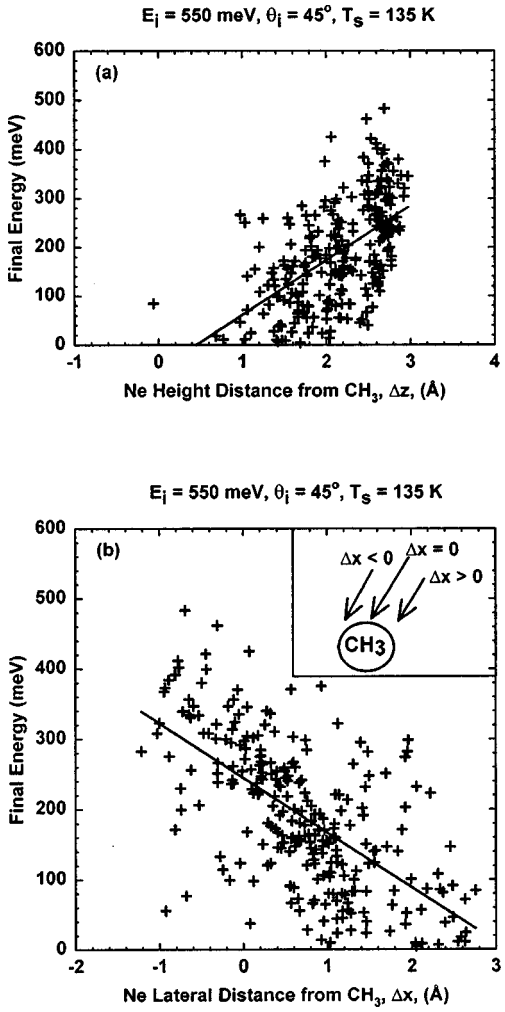

FIG. 23. Scattered Ne energy as a function of the relative Ne–CH_3 position for the nearest CH_3 at the z-turning point for single-bounce trajectories: 261 trajectories, 550 meV Ne, $\theta_i = 45°$ $\phi_i = 0°$, $T_s = 135$ K, $\phi_f = 150° - 210°$. Each point represents a trajectory. The inset panel in (a) schematically shows the lateral distance, Δx, of the Ne as it collides with the terminal methyl group. Δz, the relative Ne–CH_3 height, is always positive since with these collisions the neon does not penetrate into the monolayer.

Essential conclusions from this work are as follows:

(1) Generally good and in many instances quantitative agreement between the experimental TOF angular distributions and VENUS simulated energy distributions has been obtained under a wide range of incident neon energies, angles, and 1-decanethiol monolayer surface temperatures.

(2) Bimodal velocity distributions for incident neon energies greater than *ca.* 100 meV arise from the differing lateral distances at which the incident neon collides with the topmost portion of the SAM overlayer, as well as the configuration of the underlying methylene segments of the SAM. Large energy exchange is made possible when the neon travels into a hollow site and undergoes a direct collision with the side of a methyl group. The low energy component shows rapid and substantial accommodation with the surface; however, complete thermalization does not occur. This is demonstrated by experimental TOF fits consistently yielding a slow component temperature that is higher than the measured surface temperature. Moreover, the simulations demonstrate, as shown by examination of more than 1000 trajectories, that the vast majority of slow final trajectories arise from single-bounce encounters, i.e., they do not come from long surface-residence time events. Collisions that strike the top of the methyl groups lead to poor energy exchange and fewer subsequent surface interactions. The molecular motions that exchange energy with the neon will be discussed in another paper.[8] In addition, a minor influence on energy exchange for Ne-SAM collisions, in the energy regime discussed in this work, can be associated with the chain orientation with respect to the impinging neon atom.

(3) Most low energy (<100 meV) neon atoms undergo parallel momentum accommodation with the surface within a few picoseconds. This is in contrast to rare gas–metal surface scattering and can be attributed to the properties of the crystalline 1-decanethiol monolayer: softer and more corrugated than a metal.

In essence, the ordered SAM surface shows fast and efficient energy accommodation. This is due to both the high corrugation and the ease with which the SAMs are deformed from their equilibrium positions. As much as 60% of the incident neon energy is exchanged within a very short interaction time. In spite of this rapid accommodation little, if any, of the Ne comes off thermally equilibrated with the surface.

The validation of the numerical simulations by detailed, differential scattering measurements in this paper means that one can now predict the scattering dynamics of energetic projectiles from a variety of complex organic surfaces. This in turn implies that it is becoming a realistic goal to synthesize intentionally-structured surfaces and coatings for achieving specific energy and momentum absorption or reflection characteristics for use in technological situations including aerospace applications.

ACKNOWLEDGMENTS

This work was primarily supported by the AFOSR sponsored MURI Center for Materials Chemistry in the Space Environment. Supplemental support from the National Sci-

ence Foundation—Materials Research Science and Engineering Center at the University of Chicago is also gratefully acknowledged.

[1] T. Yan, W. L. Hase, and J. R. Barker, Chem. Phys. Lett. **329**, 84 (2000); T. Yan and W. L. Hase, Phys. Chem. Chem. Phys. **2**, 901 (2000).
[2] T. Yan and W. L. Hase, J. Phys. Chem. A **105**, 2617 (2001).
[3] S. B. M. Bosio and W. L. Hase, J. Chem. Phys. **107**, 9677 (1997).
[4] S. R. Cohen, R. Naaman, and J. Sagiv, Phys. Rev. Lett. **58**, 1208 (1987).
[5] M. E. Saecker and G. M. Nathanson, J. Chem. Phys. **99**, 7056 (1993); **100**, 3999 (1994).
[6] C. L. Berrie, Doctoral dissertation, University of California at Berkeley, Fall 1997.
[7] S. F. Shuler, G. M. Davis, and J. R. Morris, J. Chem. Phys. **116**, 9147 (2002).
[8] T. Yan, N. Isa, K. D. Gibson, S. J. Sibener, and W. L. Hase, J. Phys. Chem. A **107**, 10600 (2003).
[9] K. D. Gibson, M. Viste, E. C. Sanchez, and S. J. Sibener, J. Chem. Phys. **110**, 2757 (1999); J. I. Colonell, K. D. Gibson, and S. J. Sibener, *ibid.* **103**, 6677 (1995).
[10] J. M. Haile, *Molecular Dynamics Simulation: Elementary Methods* (Wiley, New York, 1992).
[11] P. Fenter, A. Eberhardt, K. S. Liang, and P. Eisenberger, J. Chem. Phys. **106**, 1600 (1997); F. Schreiber, Prog. Surf. Sci. **65**, 151 (2000); Y. Yourdshahyan and A. M. Rappe, J. Chem. Phys. **117**, 825 (2002).
[12] G. Liuti, F. Pirani, U. Buck, and B. Schmidt, Chem. Phys. **126**, 1 (1988).
[13] F. O. Goodman and H. Y. Wachman, *Dynamics of Gas–Surface Scattering* (Academic, New York, 1976).
[14] K. Bolton, M. Svanberg, and J. B. C. Pettersson, J. Chem. Phys. **110**, 5380 (1999).
[15] J. Harris, in *Dynamics of Gas–Surface Interactions*, edited by C. T. Rettner and M. N. R. Ashfold (The Royal Society of Chemistry, Cambridge, 1991).
[16] M. Head-Gordon, J. C. Tully, C. T. Rettner, C. B. Mullins, and D. J. Auerbach, J. Chem. Phys. **94**, 1516 (1991).
[17] W. H. Weinberg, in *Dynamics of Gas-Surface Interactions*, edited by C. T. Rettner and M. N. R. Ashfold (The Royal Society of Chemicstry, Cambridge, 1991), p. 171.
[18] U. Harten, J. P. Toennies, and C. Woell, Springer Series in Surface Sciences **3** (Dynamical phenomena at surfaces, interfaces, and superlattices: Proceedings of an international summer school at the Ettore Majorana Centre, Erice, Italy, July 1–13, 1984), 117 (1985).
[19] E. R. Jones, J. T. McKinney, and M. B. Webb, Phys. Rev. **151**, 476 (1966); G. A. Somorjai, *Introduction to Surface Chemistry and Catalysis* (Wiley, New York, 1994).
[20] A. Amirav, M. J. Cardillo, P. L. Trevor, C. Lim, and J. C. Tully, J. Chem. Phys. **87**, 1796 (1987); D. Kulginov, M. Persson, C. T. Rettner, and D. S. Bethune, J. Phys. Chem. **100**, 7919 (1996); J. E. Hurst, L. Wharton, K. C. Janda, and D. J. Auerbach, J. Chem. Phys. **78**, 1559 (1983); R. J. Smith, A. Kara, and S. Holloway, Surf. Sci. **281**, 296 (1993); R. J. W. E. Lahaye, A. W. Kleyn, S. Stolte, and S. Holloway, *ibid.* **338**(1–3), 169 (1995); R. J. W. E. Lahaye, S. Stolte, A. W. Kleyn, R. J. Smith, and S. Holloway, *ibid.* **307–309**, 187 (1994).
[21] C. T. Rettner, J. A. Barker, and D. S. Bethune, Phys. Rev. Lett. **67**, 2183 (1991).